npj | quantum information

Article

Published in partnership with The University of New South Wales

https://doi.org/10.1038/s41534-024-00827-8

Modeling Si/SiGe quantum dot variability induced by interface disorder reconstructed from multiperspective microscopy

Luis Fabián Peña [1,2], Justine C. Koepke[1], Joseph Houston Dycus[3], Andrew Mounce[4], Andrew D. Baczewski [5], N. Tobias Jacobson [5] ✉ & Ezra Bussmann [4] ✉

SiGe heteroepitaxial growth yields pristine host material for quantum dot qubits, but residual interface disorder can lead to qubit-to-qubit variability that might pose an obstacle to reliable SiGe-based quantum computing. By convolving data from scanning tunneling microscopy and high-angle annular dark field scanning transmission electron microscopy, we reconstruct 3D interfacial atomic structure and employ an atomistic multi-valley effective mass theory to quantify qubit spectral variability. The results indicate (1) appreciable valley splitting (VS) variability of ~50% owing to alloy disorder and (2) roughness-induced double-dot detuning bias energy variability of order 1–10 meV depending on well thickness. For measured intermixing, atomic steps have negligible influence on VS, and uncorrelated roughness causes spatially fluctuating energy biases in double-dot detunings potentially incorrectly attributed to charge disorder. Our approach yields atomic structure spanning orders of magnitude larger areas than post-growth microscopy or tomography alone, enabling more holistic predictions of disorder-induced qubit variability.

Nanoelectronic devices using Si/SiGe heterostructures to host quantum dot qubits offer robust coherence, one-/two-qubit gate fidelity, and compact device footprints compatible with Si foundry processing[1–12]. With the ultimate goal of monolithic Si integration, recent qubit research primarily utilizes epitaxial single quantum well heterostructures depicted schematically in Fig. 1a[13–20]. Briefly, typical qubit heterostructure material comprises a strained-Si (s-Si) well-layer pseudomorphically lattice-matched in-plane with surrounding relaxed $Si_{1-x}Ge_x$, $x \sim 0.3$[18,19]. Leading qubit varieties consist of two or three coupled electrostatic dots, depicted as harmonic wells in Fig. 1a, confining one or a few electrons vertically in the s-Si well by type-II band offsets, Fig. 1b, and laterally by voltages on nanoscale metal gates [top Fig. 1a][20,21]. Heterostructure growth by chemical vapor deposition (CVD) and molecular beam epitaxy (MBE) yields suitable qubit environments in the s-Si well with figures-of-merit including low metal-insulator percolation e^- densities ($<10^{11}$ cm^{-2}), and minimal nuclear spin background via ^{28}Si (spin-free) isotopic enrichment (>99.9%)[17–20]. Consequently, this material has enabled leading Si-based qubit technology demonstrations, e.g., coupling multiple high-fidelity qubits and rudimentary quantum error correction[7–12]. Investigation and understanding of salient future scale-up challenges including expected variability over qubit ensembles is timely[22–24].

Residual Si/SiGe interfacial atomic structure disorder is one cause for qubit variability[25–28]. In contrast to the ideal of flat interfaces and abrupt potentials, realistic structures include disorder, inset right side Fig. 1a, resulting in variability in qubit confinement potentials, Fig. 1b[2]. Disorder-induced qubit variability might result from intimate contact between dot electron wave functions and disordered interfaces exhibiting (1) random intermixing between miscible Si and Ge and (2) growth roughness of interfaces between the Si and SiGe layers. Factor (1) results in broader interface barrier potential, Fig. 1b, and consequent dot-to-dot variability in the valley character of low-lying orbitals, impacting both valley splitting (VS) and inter-dot tunnel or exchange couplings used to drive logic gating operations[25,29,30]. Factor (2) modifies the quantum well width, w, in Fig. 1b,

[1]Sandia National Laboratories, Albuquerque, NM 87185, USA. [2]Centre of Excellence for Quantum Computation and Communication Technology, School of Physics, University of New South Wales, Sydney, NSW 2052, Australia. [3]Advanced Microscopy, Eurofins EAG Materials Science, Raleigh, NC 27606, USA. [4]Center for Integrated Nanotechnologies, Sandia National Laboratories, Albuquerque, NM 87185, USA. [5]Center for Computing Research, Sandia National Laboratories, Albuquerque, NM 87185, USA. ✉e-mail: ntjacob@sandia.gov; ebussma@sandia.gov

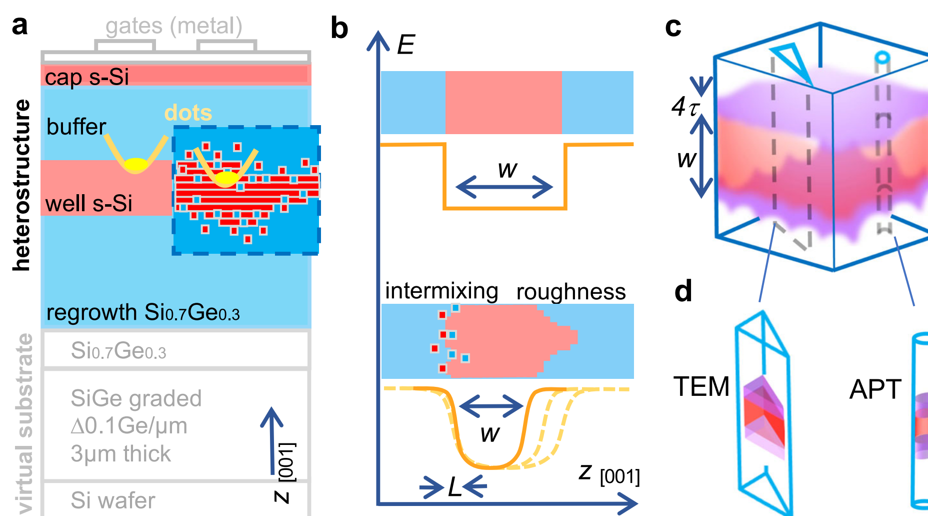

Fig. 1 | A schematic of the SiGe heterostructure in this work indicating interface disorder effects and some challenges to characterizing disorder mechanisms. **a** Qubit heterostructure schematic. The inset dashed rectangle depicts alloy and roughness disorder near interfaces. **b** An energy, E, diagram indicating that a quantum well forms in the s-Si layer owing to conduction band edge offset from adjacent SiGe layers, and the confinement potential width, w, is shaped by growth roughness and intermixing length, L. Generally, interface roughness is not strictly correlated between interfaces and intermixing may be superposed to yield **c** complex 3D interface structures that are intractable for **d** the highest spatial resolution post-growth measurement techniques, such as transmission electron microscopy (TEM) and APT owing to, e.g., limited practical measurement volumes smaller than established roughness correlation lengths, along with probe convolution effects, e.g., averaging of structure information along the TEM beam path through a cross-sectional slice. Here, 4τ denotes the observed interface width including various disorder contributions.

resulting in variation of inter-dot energy biases that might otherwise be attributed to charge disorder. For qubit operation protocols that may depend on tight control of quantum dot energy offsets, such as spin shuttling, this might serve as a nuisance source of variation that is similar in effect to but distinct in origin from charge disorder[31–34]. Stresses from fabrication or thermal expansion mismatch are another source of strain-variation-induced disorder potential[35,36].

Valley splitting variability is a focus for experiments, theory, and simulations because experiments indicate VS variability in the range 20−300 μeV[10,15,28,37–42]. This variability is significant because it is comparable to the energies separating typical qubit basis states. Therefore, valley states are a degree-of-freedom that can act as a potential leakage channel or be harnessed into new forms of qubits[15,28,37–43]. In either case, it is useful to understand and quantify VS variability.

To understand and discover control strategies for qubit-to-qubit VS variability, empirical pseudopotential, tight binding, and effective mass calculations have been useful tools[2,32]. Early work assessed VS variability starting from principled assumptions that as yet unresolved embedded interface structure consists of features, e.g., discrete mono-/bilayer- atomic-step roughness, seen on s-Si and SiGe growth surfaces with local miscuts[2,44–48]. More recently, near-atomic-resolution studies using atom-probe tomography (APT) supplemented with high-angle annular dark field scanning transmission electron microscopy (HAADF-STEM) imaging over the 10-nm-scale, show gradual interface transitions, Fig. 1b, c, and diffuse alloy disorder essentially ruling out abrupt stepped interfaces. Reported interface widths span 0.7–1.0 ± 0.3 nm, i.e., several atomic layers, with alloy number fluctuations adding variability[28,49,50]. Hence, recent theory, simulation, and experiment focus primarily on VS variability owing to random alloy disorder and alloy fluctuations[23,25,28,51].

In contrast to VS variability, which is a consequence of the particular atomic-scale alloy disorder realized in the vicinity of any given quantum dot, orbital level variability in response to disorder is comparatively straightforward to understand as a consequence of varying well width, w, Fig. 1b[2]. Well width is expected to vary owing to undulations, e.g., local growth roughness, at each interface. Prior work with hard X-ray nanospot diffraction shows roughly periodic (few-hundred-nm wavelength) lateral undulations of well width at a few atomic layer amplitude[52]. Such long-period undulation is unlikely to be connected with (Å-scale) alloy disorder and was attributed to epitaxial growth roughness. Overall, the available data hints at a qualitative structural description of the s-Si well and interfaces, including longer-period undulations (roughness) convolved with diffuse interface broadening (intermixing), as depicted in the perspective view in Fig. 1c.

Anticipating qubit-to-qubit variability owing to contributions of roughness and alloy disorder, a strategy embraced in recent works is to engineer ensemble distributions, e.g., VS distributions, over many qubits by targeted manipulation of ensemble disorder[23,25,28,51]. For example, precision placement of inherently disordered layers of Ge in or near the well is found to amplify VS[23,28]. To advance this strategy, some recent theory implementations (atomistic tight binding, empirical pseudopotential, effective mass theory) have been developed to predict structure-VS relationships from atomistic materials descriptions capturing specific disorder realizations[23,28,53]. The calculations demand accurate ensemble descriptions of buried interfaces over volumes encountered by numerous qubits sampling multiple forms of disorder. Comprehensive 3D multiscale ensemble descriptions capturing both longer-ranged undulations convolved with interfacial alloy intermixing, Fig. 1c, are intractable for individual local probing methods, e.g., HAADF-STEM and APT, Fig. 1d, owing to limited sample volumes and image convolution effects, indicating that a combination of techniques sampling across atomic-to-micrometer interface disorder realizations will yield more complete structural descriptions.

Here, we describe a multimodal, multiperspective, microscopy approach to evaluate Si/SiGe heterointerface atomic structures. Then we use the structures to model dot-to-dot (qubit) VS and orbital level (detuning) variability. The results characterize interface undulation, alloy disorder, and resulting variability of dot spectral properties over areas (>1 μm^2) characteristic of multi-qubit devices. Utilizing scanning tunneling microscopy (STM) to track MBE growth, we image surface atomic structure over micron-square areas following deposition of each heterostructure layer. STM indicates Å-to-nanometer roughness of s-Si and relaxed $Si_{0.7}Ge_{0.3}$ growth surfaces that subsequently become buried interfaces. The finished heterostructure interfaces are imaged using cross-sectional HAADF-STEM. For s-Si, STM shows atomically flat growth surfaces with atomic steps cascading monotonically along the miscut[54]. By contrast, nanometer-sized

undulations dominate SiGe surfaces owing to 2D adatom island nucleation and stacking. Post-growth HAADF-STEM imaging near regions probed by STM reveals that nanometer-sized SiGe roughness is evident at interfaces, but Å-sized structure is lost in diffuse 1.0 ± 0.4 nm-wide interfaces. Prior surface dynamics studies report atomistic mechanisms, e.g., Si-Ge surface exchange diffusion and wetting layer overgrowth, that implicate atomic-scale Si-Ge intermixing in growth yielding diffuse interfaces[55–63]. STM and HAADF-STEM are reconciled to yield an overall atomic-structure description intractable to prior reported approaches using individual local-probe techniques, e.g., HAADF-STEM or APT alone[28,49]. We use our structure data within atomistic multi-valley effective mass theory to calculate dot-to-dot variability including well thickness variation-induced inter-dot energy biases and valley splitting statistics. We predict a spread of electronic conduction band valley splittings of 0−200 μeV, which is consistent with available experimental VS measurements on qubits[10,15,28,37–42]. Also, we use our data to estimate inter-dot bias spatial variability owing to interface roughness modulating quantum well confinement along the growth axis by up to tens of meV for typical well thicknesses (5−10 nm). We are not aware of such a broad-range ensemble structure-properties description at the atomic-resolution limit in both measurement and modeling having been reported previously. Both model findings related to VS and orbital variability have significance for understanding performance limits in quantum computing applications.

Results

Experiment, SiGe growth & atomic structure measurements

Our growth study follows a layer sequence in Fig. 2a. The Methods section describes material preparation and growth, while Supplementary Methods 1 describes STM image acquisition, and Supplementary Figs. 1.1–1.4 describe the STM image analysis.

Si/SiGe MBE on relaxed, epi-ready, $Si_{0.7}Ge_{0.3}$ virtual substrates started by depositing a 70 nm-thick SiGe regrowth layer. STM images, Fig. 2b and c, indicate that the regrowth surface undulates at the nanometer scale [0.54 nm root-mean-square (RMS) roughness]. Sparse metastable pits appear occasionally, Fig. 2c. Similar pits are associated with threading dislocations terminating at the surface, although we see no indication of dislocations reaching the heterostructure layers in post-growth HAADF-STEM images[64–66].

Next, a ~15 nm-thick s-Si well was deposited on the SiGe regrowth layer. Comparing STM data, Fig. 2b, c, the well's atomically flat surface [0.18 nm roughness] is totally different from the undulating regrowth surface. The s-Si and SiGe have qualitatively different growth dynamics. The s-Si grows primarily in step-flow mode characterized by atomic steps cascading monotonically down the local miscut with few adatom islands, while SiGe grows primarily in an adatom island nucleation and stacking mode, with numerous adatom islands visible, leading to undulations and roughness. Such roughening might be favored by elastic effects owing to near-surface Ge-enrichment in MBE[67].

Note that our 15 nm-thick s-Si well exceeds the Matthews-Blakeslee critical thickness (8.5 nm for 1.3% tensile s-Si), favoring relaxation[68]. Studies indicate some small relaxation (0.01%) at 10 nm thickness[68]. However, the well surface is dominated by features that are most consistent with ~1.3% tensile-strained, versus relaxed Si[69,70]. There are sawtooth-like step fluctuations and a tendency for step bunching, indicative of competition between underlying strain fields, step energies, and surface stress[65,69,71–74]. That the well indicates tensile strain features at 15 nm-thick is consistent with observations that efficient relaxation (>0.01%) occurs above the Freund (dislocation unblocking) critical thickness (>30 nm for 1.3% tensile s-Si)[68,75].

Following well growth, a 45 nm-thick SiGe buffer layer was deposited. Buffer surface structure, Fig. 2c, resembles the SiGe regrowth layer, e.g., there are nanosized surface undulations and some sparse pit-like artifacts[70]. An increase in surface roughness compared to the well is evident (see Supplementary Figs. 1.5, 1.6)[57,76]. Finally, a 3-nm-thick Si cap was deposited.

So far, we have described growth surfaces observed via STM after each new heterostructure layer is added, prior to overgrowth and heterointerface formation. Since surface dynamics, including step mobility and intermixing are integral to growth, it is nearly certain that surfaces observed with STM change through interface formation[56,57,60,63].

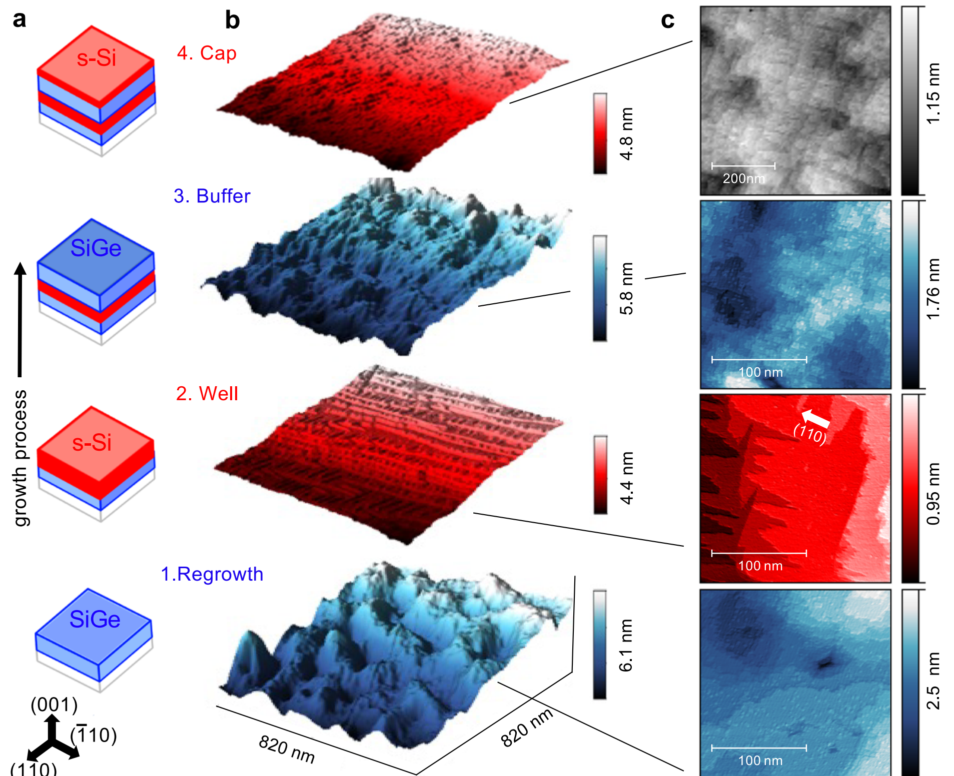

Fig. 2 | Heterostructure surface roughness imaged by STM during growth. Each column of this figure is to be read from bottom to top and shows: **a** schematic indicating heterostructure layer sequence, **b** STM images showing surface structure upon layer completion just prior to overgrowth and heterointerface formation, **c** STM images in smaller areas showing some key atomic structure features. For the upper panel, a gray scale was found to more clearly elucidate detail. STM images were acquired at −2.5 V/0.2 nA tunnel current. Note that images are obtained at similar, not identical, sites (see Supplementary Methods 1). The data has been plotted in a coordinate system defined by principal crystal directions, as indicated, for comparisons to HAADF-STEM data.

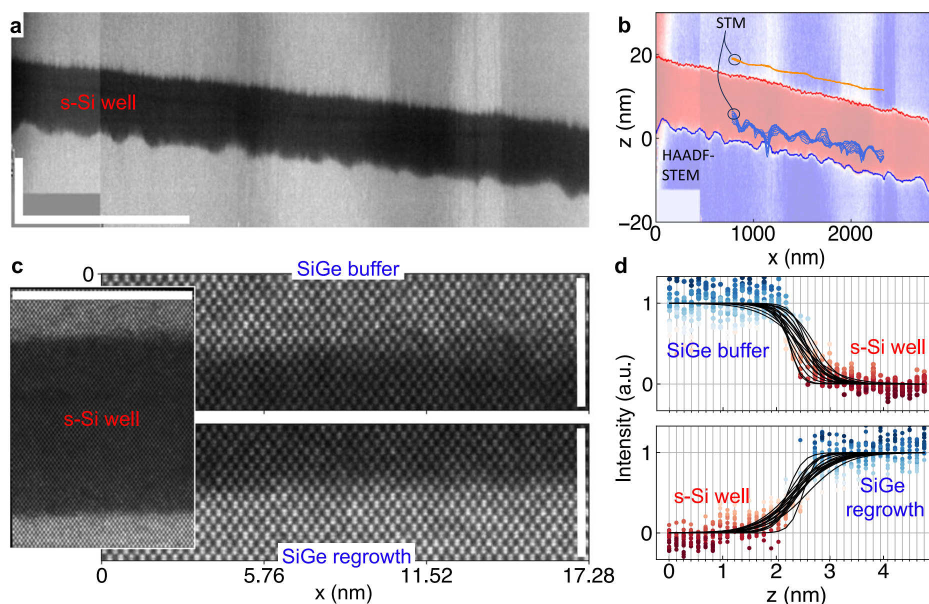

Fig. 3 | Interface disorder in post-growth cross-sectional HAADF-STEM images. a Composite image of the heterostructure. The data is plotted with a 20 × vertical scaling to emphasize nanosize interface structure. Note that STEM-EELS indicates cross-section thickness (normal to page) ranges from 20 to 120 nm thick from left-to-right. Scale bars are 15 nm vertical and 1.0 µm horizontal. **b** HAADF-STEM data plotted with a Canny edge marking and 50 × vertical scaling highlights nano-size structure similar to STM data plotted on the same scale, in the same crystal-oriented coordinate system, along $x_{i=1,2}$ = [110]-equivalent directions. **c** Atomic-resolution HAADF-STEM of the s-Si well, cropped to show heterointerfacial atomic details indicating that the interfaces are gradual at the atomic scale. Vertical scale bars are 4.5 nm. Inset shows overall image. Horizontal scale bar is 18 nm. Here, STEM-EELS indicates 22 nm lamella thickness. **d** Plots of column intensity across the interface span 7 ± 3 atomic layers on average across the image, after correcting for HAADF-STEM beam spread within the solid. The method of interface width fitting and measurement is indicated in Supplementary Methods 2.

To measure post-growth buried interface structure, we utilize cross-sectional HAADF-STEM imaging. HAADF-STEM lamella preparation, and measurements are described in the Methods section, and Supplementary Methods 2 describes the image analysis. The cross-sectional lamella imaged here is cut from a region that is near (within the same square millimeter) but not identical to STM sites. The lamella is wedge-shaped tapering from roughly 20−120 nm-thick as assessed by scanning transmission electron microscopy electron energy loss spectroscopy (STEM-EELS, Supplementary Fig. 2.1). Figure 3a shows a HAADF-STEM image of the s-Si well with adjacent SiGe layers. The data is plotted with a 20× vertical stretch (see Supplementary Fig. 2.2 for details), similar to exaggerated vertical scaling typical for STM data, to emphasize nanosized structures. HAADF-STEM intensity, I, is a probe of nuclear charge, Z, with $I \sim Z^{1.8}$, so the image contrast is an indicator for Ge content in each atomic column along the electron beam path[49]. Note that HAADF-STEM images convolve 3D structures along the beam path through the solid. Around interfaces, contrast convolves structure such as roughness, tilts, and alloy disorder.

To compare growth and post-growth features, we plot HAADF-STEM and several STM line traces encompassing similar interface area, Fig. 3b, adding markings to the HAADF-STEM interfaces. It is evident that nanoscale interface features are comparable in scale to preexisting surface features seen by STM. The lower interface has nanosized undulations from the SiGe regrowth, whereas the upper interface is relatively flat with waviness reminiscent of s-Si step-density fluctuations and bunches observed in STM. In Table 1, we compare ensemble roughness and correlation lengths for growth surfaces (STM) and corresponding post-growth interfaces (HAADF-STEM) (see Supplementary Figs. 1.5 and 2.3). Comparing each surface and corresponding interface, RMS roughnesses and correlation lengths are similar, but interfaces feature increased roughness, and decreased correlation lengths, which might indicate additional shorter-range disorder mechanisms, e.g., alloy disorder around interfaces.

Table 1 | RMS roughness and correlation lengths for the upper and lower interfaces of the well determined from surface (STM) and interface (HAADF-STEM) images

Surface/interface (microscope)	RMS roughness nanometers	Correlation length nanometers
Upper s-Si surface (STM)	0.18 ± 0.01	107 ± 33
Upper (HAADF-STEM)	0.24 ± 0.01	73 ± 16
Lower SiGe surface (STM)	0.54 ± 0.01	45 ± 13
Lower (HAADF-STEM)	0.68 ± 0.01	34 ± 9

Stated error bar is fit-parameter uncertainty.

The significant, visually apparent, observation from Fig. 3a, b is that well thickness varies appreciably owing to differing roughness of the well's upper and lower interfaces. In addition, scale-independent interface-to-interface correlations are tested by Pearson's correlation coefficient, PCC = $\mathrm{cov}(z_1, z_2)/\sigma_1\sigma_2$, where z_i denote the heights, σ_i denote the RMS roughnesses, at the lower ($i = 1$), and upper ($i = 2$) interfaces[77]. We calculate a PCC = 0.18 (perfect correlation yields PCC = 1, non-correlation yields PCC = 0) from HAADF-STEM interface positions marked in Fig. 3b, indicating little evidence for cross-correlated roughness. Note that thinner wells might have greater interface-to-interface correlation.

To image a shorter-range interface structure, we measure atomic-resolution HAADF-STEM images. Figure 3c shows one example image, see Supplementary Fig. 2.4 for more. In contrast to our STM data, HAADF-STEM shows no indication of abrupt interfaces or atomic steps, but rather gradual interfaces in Fig. 3c. From STM atomic-step observations of atomic-step spatial distributions (see Supplementary Figs. 1.7–1.9), we would expect to observe atomically-abrupt interfaces (0.134 nm interface transitions) with a finite probability of capturing at least a few steps in the 18 nm-width in Fig. 3c.

Instead, we observe interface widths spanning several atomic layers, Fig. 3d, with smooth transitions (vertically along each atomic column) reasonably estimated by sigmoid curve fits (see analysis in Supplementary Figs. 2.4–2.8). We measure the interface width using 4τ, where τ is the sigmoid width fit parameter. The parameter 4τ measures the distance for ~0.12−0.88 of the full transition, and is commonly utilized to estimate HAADF-STEM and APT interface widths[28,49]. To calculate a mean interface width $\overline{4\tau}$ comprehensive of entire images, we apply a segmentation and sigmoid fitting routine to extract an interface width, 4τ, from every vertical atomic column, then calculate a mean stated as 4τ (no overbar) (see Supplementary Fig. 2.8). Fits to all atomic columns in Fig. 3c, yield $4\tau \pm \sigma = 0.9 \pm 0.4$ nm and 1.2 ± 0.5 nm for the lower and upper interfaces, respectively. Appreciable standard deviations σ capture interface width fluctuations[28].

Interpreting HAADF-STEM interface width is complicated because contrast convolves structural information along the electron beam path[49].

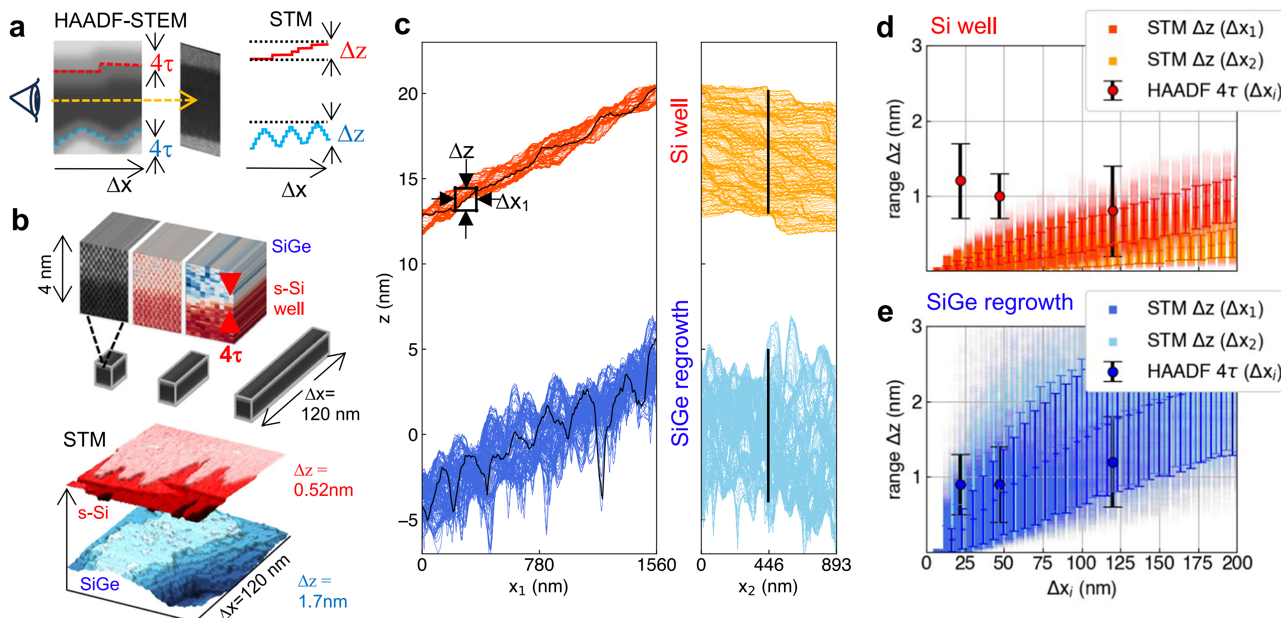

Fig. 4 | Analysis of interface disorder contributions from roughness (STM) and intermixing (HAADF-STEM). **a** A drawing showing that HAADF-STEM cross-sectional views yield interface widths, 4τ, convolving interface roughness (Δz) with other structures, e.g., alloy disorder (soft gray scale). To account for roughness contributions, we use our STM data to estimate Δz distributions for comparison to 4τ values. **b** An outline of our technique depicting three volumes, $\Delta x = 22$, 47, and 120 nm, imaged with the HAADF-STEM beam directed along Δx. Each image volume is analyzed to yield an interface width $4\tau \pm \sigma$. At lower left there are STM images from the s-Si (red) and SiGe (blue) to give some idea of the preexisting roughness features, $\Delta z(\Delta x \le 120)$nm. Note flat s-Si atomic layers versus SiGe islanding. **c** Two orthogonal views of the STM data used to calculate ensemble roughness, plotted in the crystal-oriented coordinates with (001) as the z axis and (110)-directions aligned to $\Delta x_{i=1,2}$. A single line is plotted in black to indicate directional relationships in the two orthogonal views. **d** s-Si well-to-buffer interface width vs. lamella thickness (Δx) characterized by HAADF-STEM 4τ and surface width contributions, Δz, from STM data along $\Delta x_{i=1,2}$ orientations. **e** SiGe regrowth-to-Si well interface width vs. lamella thickness (Δx) characterized by HAADF-STEM 4τ with Δz. All error bars indicate one standard deviation from the mean.

Transiting the solid, a beam encounters various features (roughness, alloy disorder), yielding a projected image with intensity averaging composition, Fig. 4a. Since STM images indicate roughness alone, we utilize the STM data to estimate roughness contributions (Δz) to the interface width. By comparing Δz distributions to measured 4τ we can test whether roughness alone, or additional effects, are likely to explain the interface widths. Note that roughness contributions to HAADF-STEM interface widths are expected to become negligible for lamella thickness << correlation length for roughness.

To implement this idea, we take an approach of measuring 4τ as a function of a few lamella thicknesses ($\Delta x = 22$, 47, and 120 nm, see Supplementary Fig. 2.4) and comparing the $4\tau(\Delta x)$ to $\Delta z(\Delta x)$ calculated from STM data. The approximate HAADF-STEM sample volumes are depicted in Fig. 4b with similar-sized STM examples for comparison. The measured interface widths, $4\tau \pm \sigma$, for each lamella thickness, are indicated in Table 2.

Next, we estimate interface width contributions due to preexisting surface roughness and tilts in STM data. We use a metric $\Delta z = \max(z) - \min(z)$, that we refer to as the range function, calculated over intervals, $\Delta x_{i=1,2}$ along (110)-equivalent directions in the STM data, i.e., along the same directions probed by HAADF-STEM. The $\Delta x_{i=1,2}$ span the lamella thicknesses. By rastering the $\Delta x_{i=1,2}$ window over micron-sized STM data, Fig. 4c, a micron-scale characteristic ensemble estimate for $\Delta z(\Delta x_{i=1,2})$ is calculated, Fig. 4d, e.

Table 2 | Interface widths 4$\tau \pm \sigma$ in our atomic-resolution HAADF-STEM data

Lamella thickness:	22 nm	47 nm	120 nm
Upper interface width	1.2 ± 0.5 nm	1.0 ± 0.3 nm	0.8 ± 0.6 nm
Lower interface width	0.9 ± 0.4 nm	0.9 ± 0.5 nm	1.2 ± 0.6 nm

For the s-Si well surface (well upper interface) Fig. 4d, values of $4\tau(\Delta x = 22, 47\text{ nm})$ lie outside the Δz distribution. These values can not be attributed to roughness and miscut (interface slope) and can only be understood if other disorder, e.g., alloy disorder, is present. By contrast, for the SiGe regrowth surface (well lower interface) Fig. 4e, all 4τ values fall within the Δz distribution, and can be attributed primarily to growth roughness and miscut.

We postulate that alloy disorder, arising from intermixing, is a plausible explanation for the anomalous upper interface widths $4\tau(\Delta x) = 1.2 \pm 0.5$ nm and 1.0 ± 0.3 nm, at $\Delta x = 22$, 47 nm, that can not be explained by preexisting roughness. To estimate a characteristic intermixing length, L, we calculate, $L = [4\tau^2 - \Delta z^2]^{1/2}$, where the Δz values (0.04−0.25 nm) contribute negligibly, and we conclude that 0.9 nm < L < 1.2 nm (±0.4 nm) or 7−9(± 3) layers.

Discussion

Si and Ge are fully bulk miscible, and there are a few surface/near-surface mechanisms that are likely to be active allowing Ge to intermix with the Si over multiple atomic layers, as well as allowing Si transport upward from the original interface[55–63]. First, there is a near-surface enhanced interstitial mechanism of Uberuaga et al. that allows transport of appreciable Ge up to 4 atomic layers below the original Si growth surface for $T \le 500$ °C[56]. Second, intuitively consistent with bulk Si-Ge miscibility, SiGe alloys form a 2D surface wetting layer on Si surfaces by purely surface atomic exchange diffusion processes, leading to an upward exchange of atoms from surface lattice sites to the supersaturated gas of adatoms involved in growth, and ultimately into subsequent atomic layers as they nucleate. Surface exchange diffusion is rapid at $T > 90$ °C for Si and Ge and anticipated to contribute significantly to intermixing at increasing temperatures[57,58,63]. If atomic exchange diffusion promotes Si upward with a probability $p \sim 0.5$, then we anticipate additional Si to be distributed upward to the nth layer above the

original growth surface with a probability p^n, such that layers above the original Si surface become Si-rich in a diminishing, roughly geometric, progression and plausibly contribute a few additional intermixed layers to the observed 4τ[57,58,63]. Hence, we conclude that the intermixing length 7−9 atomic layers is at least possible as an outcome of prior established surface intermixing processes during growth. Finally, note that broadening effects are not limited to the upper interface, rather they are definitively resolvable and quantifiable there for thinner lamella (22, 47 nm thick).

Currently, most SiGe qubit materials are supplied by CVD growth, so we compare our results with relevant CVD materials data[28,49,52]. Generalized MBE-to-CVD comparisons are challenging since there are many variables in CVD techniques and recipes. Regarding s-Si/SiGe interface widths, our well upper interface width, $4\tau \pm \sigma = 1.0 \pm 0.4$ nm, is comparable to 0.85 ± 0.32 nm and 0.79 ± 0.31 nm using APT in ref. [28], and 0.75 nm (APT) and 0.72 nm (HAADF-STEM) in ref. [49]. Appreciable width fluctuations (0.3–0.4 nm) that modify valley splittings also compare well[28]. For the well's lower interface, we obtain $4\tau \pm \sigma = 1.0 \pm 0.5$ nm while ref. [49] reports 0.96 nm (APT), and 1.03 nm (HAADF-STEM). In recent CVD growth studies to be detailed in future publications, we find that 70 nm-thick SiGe regrowth material (optimized growth $T = 600$ °C) has 0.2 nm RMS roughness, versus 0.54 nm here ($T = 550$ °C MBE). It is not clear that CVD includes a Ge-enriched surface layer thought to impede diffusion and promote elastic roughening in MBE[67]. By comparison, for our 10 nm-thick CVD s-Si wells ($T = 600$ °C growth), RMS roughness is 0.1–0.2 nm which is similar to 0.18 nm MBE roughness. Somewhat smaller undulations in CVD more closely align to Evans et al.'s X-ray diffraction showing lateral well-width undulations at few atomic layer amplitude[52]. Note that the smaller roughness in optimized CVD growth processes might reduce orbital energy variability.

Given our STM and HAADF-STEM observations, we propose a model for atomic structure for the well where the mean position $\bar{z}(x_1, x_2)$ of each interface at a given location (x_1, x_2) is set by the STM data and the elemental identity at each lattice site along atomic columns across the interface is determined by drawing from the sigmoid distribution with a width set by HAADF-STEM data. In our atomistic multi-valley effective mass theory simulations, for any given alloy realization we construct a bulk silicon (diamond) lattice encompassing the simulation domain and then update the Si or Ge identity of each lattice site according to the above distribution. These structures are available from the authors on request.

Interface topographic data from both HAADF-STEM [Fig. 3a, b] and STM [Fig. 4c] indicate that the well thickness varies significantly across the sample, on the scale of a few nm. For example, the well width in the HAADF-STEM data [Fig. 3a, b] fluctuates by a root-mean square deviation of 1.7 nm. The well thickness sets the energy scale of confinement along the growth axis of an electron in a quantum dot. For a given quantum dot, this amounts to an overall offset that, for a double- or multi-quantum dot system, will manifest as an inter-dot energy offset (detuning) bias. To model the consequences of well thickness variation, we solve the one-dimensional Schrödinger equation for various well thicknesses, including the potential induced by the conduction band offsets between the s-Si well and SiGe layers as well as interface thickness 4τ, assumed here to be 1 nm [Fig. 5a]. The confinement energy as a function of well thickness is shown in Fig. 5b. We find that the scale of variation of vertical confinement depends significantly on the mean well thickness, with thinner wells manifesting much larger fluctuations in vertical confinement. To estimate the effect of well thickness variation on the detuning bias offset between nearby double quantum dots, we use the measured variation of well thickness shown in Fig. 5c and assumption of a 5 nm average well thickness to find the detuning bias variation of Fig. 5d for quantum dots having a nominal 80 nm center-to-center separation. For relatively thin wells (~5 nm), this simulated level of detuning bias variation would correspond to significant offsets in, for example, the voltage bias on applied gate electrodes required to induce an inter-dot transition of an electron. Such variation may otherwise be attributed to charge disorder, but we point out here that well thickness variation may be another source of bias variation to consider. If growth of the s-Si well is closer to conformal for thinner interfaces, we would expect that variation of the well thickness may be correspondingly reduced.

To probe disorder impacts on valley splitting, we perform multi-valley effective mass theory simulations of single-electron quantum dots in the presence of atomistic disorder corresponding to specific alloy realizations. Our simulation method incorporates detailed Bloch functions derived from density functional theory (DFT)[78] and treats each Ge atom in the simulation domain explicitly as a repulsive localized defect potential (see Methods). In Fig. 6a, we show the distribution of valley splitting as a function of interface width 4τ for a 5 nm-thick well, for three different cases of step structure. In these calculations, we assume harmonic confinement in the x-y plane corresponding to a 1.5 meV orbital splitting. We consider a step oriented along the [110] axis that is m atomic monolayers thick and passing through the center of the quantum dot. For the case of zero intermixing (perfectly abrupt interface), we find that the presence of the step modulates the valley splitting significantly, though the valley splitting remains relatively high (~1 meV) on average. However, as the interface width grows the influence of the step rapidly vanishes, with even a relatively abrupt interface of $4\tau = 0.5$ nm exhibiting negligible step-induced modulation of valley splitting.

Next, we explore how the valley splitting depends on well thickness. In Fig. 6b, we show how the valley splitting statistics depend on well thickness

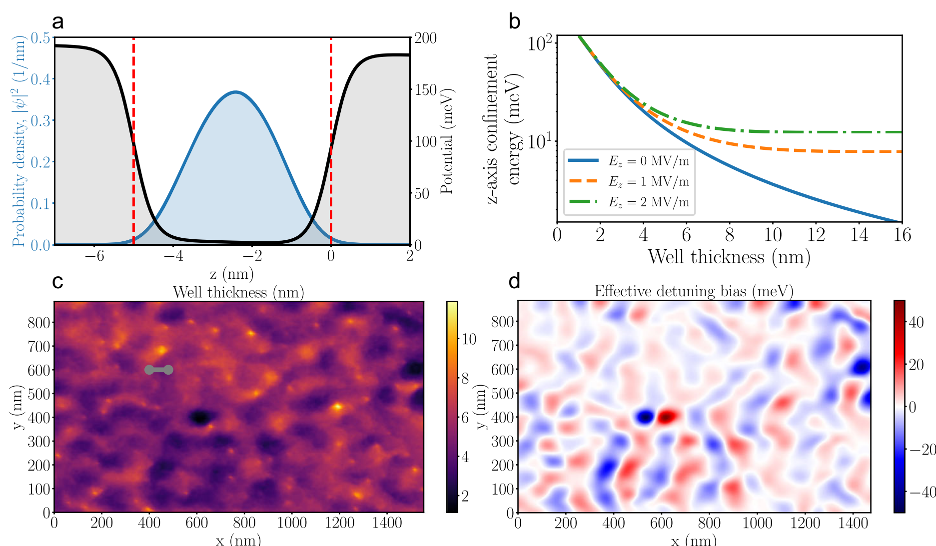

Fig. 5 | Influence of interface topography variation and confinement along the growth axis. a Example one-dimensional (valley-free) Schrödinger solve for the ground state, illustrating quantum confinement along the growth axis (z axis) of the well. Here, the quantum well is 5 nm thick, with an intermixing length of $4\tau = 1$ nm and vertical electric field of 1 MV/m. **b** Confinement energy as a function of well thickness for $4\tau = 1$ nm and various vertical electric field strengths. **c** Well thickness as a function of x,y position in the measured sample, assuming an average thickness of 5 nm and topography measured for the 15 nm sample. A pair of quantum dots 30 nm in diameter and 80 nm apart is denoted in gray to give a sense of scale. **d** Calculated effective detuning bias between dots 80 nm apart in a 5 nm well due to spatial variation of the growth axis confinement energy, assuming a vertical electric field of 1 MV/m.

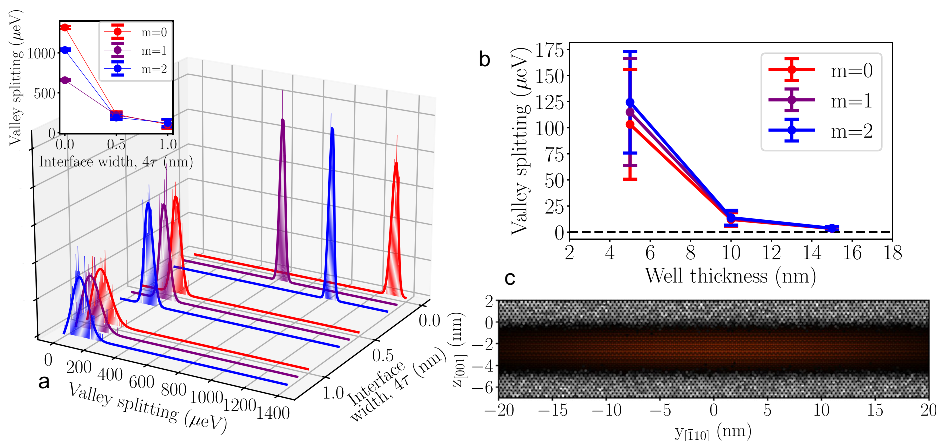

Fig. 6 | Dependence of valley splitting on alloy disorder and interface steps. Simulations of quantum dot valley splitting in the presence of alloy disorder and interfacial steps, assuming in-plane harmonic confinement corresponding to an orbital splitting of 1.5 meV. **a** For a 5 nm-thick well, distributions of valley splitting as a function of interface width (intermixing length) 4τ in the presence of either no step ($m = 0$), a single monoatomic layer ($m = 1$), or two monoatomic layer ($m = 2$) steps through the middle of the dot oriented along the [110] crystallographic axis. The solid curves are best-fit Rice distributions[28]. **b** Valley splitting statistics as a function of well thickness for each of these step configurations, **c** Example simulation of quantum dot probability density $|\Psi|^2$ for a 5 nm well, superimposed on a simulated HAADF-STEM image of Ge concentrations for a lamella 20 nm-thick parallel to the [110] plane. Error bars indicate standard deviation.

in the presence of an m-monolayer atomic step through the center of the dot, in the case of an interface width of $4\tau = 1$ nm. Well thickness clearly has a significant influence over valley splitting, with thinner wells clearly preferable to thicker wells and the presence of the few-monolayer step having minimal influence over the valley splitting distribution. In Fig. 6c, we show the electronic wave function for a 5 nm well, along with a simulated HAADF-STEM image of Ge alloying analogous to Fig. 3c. These simulations emphasize the critical importance of small well thickness and relatively abrupt interfaces in ensuring large valley splitting, while for realistic intermixing lengths the influence of few-monolayer steps is modest.

In summary, we analyze interfacial atomic structure disorder for s-Si quantum wells bounded by $Si_{0.7}Ge_{0.3}$ layers utilizing atomic-to-micron-scale data from in-operando/in-situ STM interleaved with MBE growth, and post-growth HAADF-STEM. STM images of each heterostructure layer immediately prior to overgrowth and interface formation show s-Si surfaces with atomic steps cascading essentially monotonically along local miscuts indicative of a predominantly step-flow (Frank-van der Merwe) growth mode. By contrast, SiGe surfaces show 2D nucleation, island-stacking, and Stranski-Krastanov-like growth causing nanosized roughness[67]. To investigate post-growth structure, we utilize cross-sectional HAADF-STEM measurements, that indicate that nanoscale trends of flat s-Si versus undulating SiGe persist, but that interfaces appear broadened by 1.0 ± 0.4 nm. Growth roughness does not fully explain the broadening. Instead, another mechanism must be operative, which we identify as Si-Ge intermixing reflecting miscibility accessed via surface/near-surface atomistic paths[56,57,60,63]. Utilizing STM and HAADF-STEM data, we propose an overall atomic structure with the mean interface position $\bar{z}(x_1, x_2)$ set by the STM data and the Ge distribution set by drawing from a sigmoidal distribution with HAADF-STEM $4\tau = 1.0(\pm 0.4)$nm. Our model extends interface structure descriptions by orders-of-magnitude in area ($<100 \times 100$ nm^2 to $>1 \times 1$ μm^2). Notably, we find roughness autocorrelation lengths (45–107 nm) that are up to 3 times larger than the dimensions of the data (APT/HAADF-STEM) used in other recent studies, underlining that our approach reveals broader information[28,49].

Next, we utilize our structures to estimate growth axis confinement energy and valley splitting variability for quantum dots in the s-Si layer. Confinement energy is calculated using a straightforward effective mass theory solution for the ground state confinement energies which vary owing to well-width variability resulting from uncorrelated roughness at Si/SiGe surfaces. We find that this interfacial roughness leads to appreciable confinement energy variability in our simulations of tens of meV for a 5-nm-thick well. This implies added complexity in realizing e.g., spin shuttling, requiring either coordinated manipulation of the electrostatic potential landscape or more aggressive control amplitudes to overcome disorder[33]. Valley splitting varies appreciably, e.g., in the range of 0–200 μeV for a 5-nm-thick well with $4\tau = 1$ nm interface width. This significant VS variability presents similar measurement challenges. Mitigation strategies for VS variability have been proposed, e.g., positioning Ge layers strategically in the well or near interfaces to regularize valley-state phases and break degeneracies[2,23,28].

We anticipate our imaging method and model to be useful in understanding outcomes of such strategies. We caveat that growth mechanisms and disorder realizations depend on growth recipes, and case-by-case results are not entirely likely to be generalizable. For example, we find CVD SiGe growth roughness somewhat smaller (0.2 nm versus 0.54 nm) than MBE, which might reduce confinement energy variability. Instead, this work should be understood to show an approach to isolate atomistic disorder mechanisms via coordinated multiscale, multiperspective, structure data, and then estimate their impact on qubit variability.

Methods

SiGe growth study with STM imaging

Our growth study was performed on $Si_{0.7}Ge_{0.3}$ virtual substrates (*Lawrence Semiconductor Research Labs*) with a linearly graded layer (Ge fraction increasing at ~10%/μm to 3 μm-thick) and a 600 nm-thick constant-composition top layer. Samples were cleaned (sonication in dichloromethane, acetone, and methanol and deionized water), immersed in 47% HF for 30 seconds, then rinsed in deionized water. In vacuum at 2×10^{-10} Torr, samples were annealed to 350 °C and exposed to 18000 L of atomic hydrogen. Growth was done in a MBE tool coupled to a STM in adjacent ultrahigh vacuum chambers (*Scienta Omicron Lab10 MBE, VT STM*). Heterostructure growth was performed at a deposition rate of 1 nm/minute, and substrate T = 550 °C measured by band edge thermometer (*BandIT, KSA Inc.*). Si flux is supplied by a rod-fed electron beam source (*Thermionics Inc.*) with Ge flux from a thermal cell (*MBE Komponenten*). Rate control is via a quartz crystal monitor) and alloys have ~10% composition variability assessed via secondary ion mass spectrometry (SIMS). Following each heterostructure layer, Supplementary Fig. 1.1, we performed STM imaging (tunnel current $I = 0.2-0.5$ nA, tip bias -2.0 to -2.5 V) at a few sites on the sample. Note that for each layer, STM images are obtained at slightly differing sites, i.e., this is not a precise coincident-site study.

Post-growth HAADF-STEM imaging

A HAADF-STEM lamella was prepared using ion milling and lift-out techniques by a *ThermoFisher Scientific Helios Nanolab 660* dual-beam focused ion beam with final thinning performed at 1 keV using Ga as the milling species. Lamella thicknesses were estimated by STEM-EELS using the log-ratio method. HAADF-STEM images were acquired with a *Hitachi HD2700* probe-corrected STEM using an electron beam energy of 200 keV with detector inner and outer angles of 65 mrad and 271 mrad, respectively.

Valley splitting calculations

To calculate quantum dot properties such as valley splitting in the presence of posited atomistic disorder configurations, we employ three-dimensional multi-valley effective mass theory[78]. We treat each Ge atom in the simulation domain as a repulsive localized potential, with the resulting inter- and intra-valley matrix elements arising from this localized potential acting on DFT-derived plane-wave representations of the unstrained bulk Si conduction band minima Bloch functions[78]. We scale the strength of this localized potential to reproduce the band offset between the Si well and surrounding SiGe layers. Given a conduction band offset of ~180 meV for 30% Ge[17,79], we attribute to a single Ge atom located at a diamond lattice site $\mathbf{R}_i$ the potential $V_{\mathrm{Ge}}(\mathbf{r}) = \alpha\delta^{(3)}(\mathbf{r}-\mathbf{R}_i)$. Given the volume per lattice site $a_0^3/8 \approx 0.02\ \mathrm{nm}^3$ for lattice constant $a_0 = 0.543$ nm, we set the value of the potential prefactor to be $\alpha = 12\ \mathrm{meV\ nm}^3$.

For a potential $V(\mathbf{r})$, the intra- and inter-valley matrix elements between envelope functions ϕ_μ and ψ_ν are given by

$$\langle\phi_\mu|\hat{V}|\psi_\nu\rangle = \int \mathrm{d}^3\mathbf{r}\,\phi_\mu^*(\mathbf{r})\psi_\nu(\mathbf{r})u_\mu^*(\mathbf{r})u_\nu(\mathbf{r})e^{i(\mathbf{k}_\nu-\mathbf{k}_\mu)\cdot\mathbf{r}}V(\mathbf{r}), \quad (1)$$

with $u_\mu(\mathbf{r}) = \sum_{\mathbf{G}} c_{\mu,\mathbf{G}} e^{i\mathbf{G}\cdot\mathbf{r}}$ being the lattice-commensurate part of the Bloch function for valley μ and $\mathbf{k}_\mu$ being the position of the corresponding conduction band minimum. The reciprocal lattice vectors are $\mathbf{G} = (2\pi/a_0)(i, j, k)$ for $i, j, k \in \mathbb{Z}$. The plane-wave representations of the Bloch functions that we use are those previously reported[78]. In the case of the δ-localized potential $V_{\mathrm{Ge}}(\mathbf{r})$ assumed to arise from a single substitutional Ge atom in the lattice, we must sum over all reciprocal lattice vectors $\mathbf{G}$. We find

$$u_{\pm z}^*(0)u_{\pm z}(0) = \sum_{\mathbf{G},\mathbf{G}'} c_{\pm z,\mathbf{G}'}^* c_{\pm z,\mathbf{G}} \approx 0.95 \quad (2)$$

$$u_{\mp z}^*(0)u_{\pm z}(0) = \sum_{\mathbf{G},\mathbf{G}'} c_{\mp z,\mathbf{G}'}^* c_{\pm z,\mathbf{G}} \approx 0.98, \quad (3)$$

where we neglect terms in the sum over reciprocal lattice vectors where $\|\mathbf{G}-\mathbf{G}'\| > 6.3(2\pi/a_0)$ to minimize k-space truncation effects from the available DFT-derived plane-wave representation of the Bloch functions.

We use an interior penalty discontinuous Galerkin discretization[80] of the Shindo-Nara equations, with a modal basis consisting of tensor products of Legendre polynomials up to third order on a hexahedral mesh (giving $4^3 = 64$ modal basis states per mesh element) with edge lengths 24 (30) nm in the x-y plane for the 5 (10, 15) nm well thickness cases, respectively, and 0.45 nm along the z axis to capture the details of wavefunction penetration into the interfaces. Our mesh refinement and modal basis order are chosen based on tests of convergence of eigenenergies to within few μeV for representative alloy disorder realizations. The time to solution for each eigensolve requires order 10 minutes on a single 2.6 GHz Intel Sandy Bridge CPU core. The resulting sparse matrix representation of the localized potential arising from a Ge atom is efficiently evaluated as a sum of products of Legendre polynomials. The aggregate generalized eigenvalue problem is solved using the locally optimal block preconditioned conjugate gradient (LOBPCG) method using a Jacobi preconditioner. In our sparse eigensolves we compute the lowest four eigenstates.

In our calculations, we assume isotropic harmonic confinement in the x-y plane of 1.5 meV, a scale consistent with typical observed orbital splittings of $\mathcal{O}(1)$ meV[28,37]. We assume a vanishing vertical electric field, though in practice details of tuning and device geometry may result in an electric field that preferentially biases the quantum dot towards one interface or another[28].

Variable confinement along growth axis

To model the effect of variable well thickness on quantum dot energetics, particularly as relevant to governing relative energetics in double- or multi-dot systems, we solve the 1d Schrödinger equation describing a conduction band electron in a finite quantum well with a profile given by the HAADF-STEM-derived interdiffusion length 4τ, see Fig. 4d, e. To straightforwardly capture the dependence of quantum dot energies arising from well thickness variation, for these calculations we neglect valley physics. Our 1d calculations entail a simple finite-difference discretization of the single-electron Schrödinger equation in a finite well having effective mass $m_\parallel = 0.98m_0$,

$$\left(-\frac{\hbar^2}{2m_\parallel}\frac{\partial^2}{\partial z^2} + V(z)\right)\psi(z) = E\psi(z), \quad (4)$$

with $V(z)$ capturing the effects of band offset V_0 at the interface between Si and SiGe layers and electric field F as

$$V(z) = \frac{V_0}{2}\left(2 + \tanh\left(-\frac{z+w}{\sigma_l}\right) + \tanh\left(\frac{z}{\sigma_u}\right)\right) - Fz, \quad (5)$$

with w the well thickness and V_0 again assumed to be ~180 meV for $\mathrm{Si_{0.7}Ge_{0.3}}$. In our calculations we assume $\sigma_l = \sigma_u = \sigma$, with $\sigma = (4\tau)/2$ as in the main text.

In Supplementary Fig. 3.1, we show additional examples of the effects of vertical electric field on wavefunction localization for thicker (10 and 15 nm) wells. In Supplementary Fig. 3.2, we show how the distribution of confinement energy along the growth axis depends on vertical electric field and well thickness.

Since quantum dots have finite lateral (in-plane) dimensions and will consequently sample a finite area of the interfaces, in our variable confinement calculations, we convolve the upper and lower interfaces with a Gaussian standard deviation $\sigma = 15$ nm, approximately the dimensions of a typical quantum dot.

Data availability

The data sets that support the findings of the present study will be available from the corresponding authors via email upon request. All the custom code developed for this study will be available from the corresponding author via email upon request.

Received: 27 August 2023; Accepted: 7 March 2024;
Published online: 27 March 2024

References

1. Maune, B. M. et al. Coherent singlet-triplet oscillations in a silicon-based double quantum dot. *Nature* **481**, 344–347 (2012).
2. Zwanenburg, F. A. et al. Silicon quantum electronics. *Rev. Mod. Phys.* **85**, 961–1019 (2013).
3. Kawakami, E. et al. Electrical control of a long-lived spin qubit in a Si/SiGe quantum dot. *Nat. Nanotechnol.* **9**, 666–670 (2014).
4. Zajac, D., Hazard, T., Mi, X., Nielsen, E. & Petta, J. R. Scalable gate architecture for a one-dimensional array of semiconductor spin qubits. *Phys. Rev. Appl.* **6**, 054013 (2016).
5. Yoneda, J. et al. A quantum-dot spin qubit with coherence limited by charge noise and fidelity higher than 99.9%. *Nat. Nanotechnol.* **13**, 102–106 (2018).
6. Yang, C. et al. Silicon qubit fidelities approaching incoherent noise limits via pulse engineering. *Nat. Electron.* **2**, 151–158 (2019).
7. Mills, A. R. et al. Two-qubit silicon quantum processor with operation fidelity exceeding 99%. *Sci. Adv.* **8**, eabn5130 (2022).
8. Noiri, A. et al. Fast universal quantum gate above the fault-tolerance threshold in silicon. *Nature* **601**, 338–342 (2022).
9. Xue, X. et al. Quantum logic with spin qubits crossing the surface code threshold. *Nature* **601**, 343–347 (2022).
10. Philips, S. G. et al. Universal control of a six-qubit quantum processor in silicon. *Nature* **609**, 919–924 (2022).
11. Takeda, K., Noiri, A., Nakajima, T., Kobayashi, T. & Tarucha, S. Quantum error correction with silicon spin qubits. *Nature* **608**, 682–686 (2022).

12. Weinstein, A. J. et al. Universal logic with encoded spin qubits in silicon. *Nature* **615**, 817–822 (2023).
13. Sakr, M. R., Jiang, H. W., Yablonovitch, E. & Croke, E. T. Fabrication and characterization of electrostatic Si/SiGe quantum dots with an integrated read-out channel. *Appl. Phys. Lett.* **87**, 223104 (2005).
14. Goswami, S. et al. Controllable valley splitting in silicon quantum devices. *Nat. Phys.* **3**, 41–45 (2007).
15. Borselli, M. G. et al. Measurement of valley splitting in high-symmetry Si/SiGe quantum dots. *Appl. Phys. Lett.* **98**, 123118 (2011).
16. Lu, T.-M. et al. Enhancement-mode buried strained silicon channel quantum dot with tunable lateral geometry. *Appl. Phys. Lett.* **99**, 043101 (2011).
17. Schäffler, F. High-mobility Si and Ge structures. *Semicond. Sci. Technol.* **12**, 1515 (1997).
18. Richardson, C. J. & Lee, M. L. Metamorphic epitaxial materials. *MRS Bull.* **41**, 193–198 (2016).
19. Scappucci, G., Taylor, P., Williams, J., Ginley, T. & Law, S. Crystalline materials for quantum computing: Semiconductor heterostructures and topological insulators exemplars. *MRS Bull.* **46**, 596–606 (2021).
20. Gyure, M. F., Kiselev, A. A., Ross, R. S., Rahman, R. & Van de Walle, C. G. Materials and device simulations for silicon qubit design and optimization. *MRS Bull.* **46**, 634–641 (2021).
21. Eng, K. et al. Isotopically enhanced triple-quantum-dot qubit. *Sci. Adv.* **1**, e1500214 (2015).
22. Dodson, J. et al. How valley-orbit states in silicon quantum dots probe quantum well interfaces. *Phys. Rev. Lett.* **128**, 146802 (2022).
23. McJunkin, T. et al. SiGe quantum wells with oscillating Ge concentrations for quantum dot qubits. *Nat. Commun.* **13**, 1–7 (2022).
24. Martinez, B. & Niquet, Y.-M. Variability of electron and hole spin qubits due to interface roughness and charge traps. *Phys. Rev. Appl.* **17**, 024022 (2022).
25. Neyens, S. F. et al. The critical role of substrate disorder in valley splitting in Si quantum wells. *Appl. Phys. Lett.* **112**, 243107 (2018).
26. Tariq, B. & Hu, X. Effects of interface steps on the valley-orbit coupling in a Si/SiGe quantum dot. *Phys. Rev. B* **100**, 125309 (2019).
27. McJunkin, T. et al. Valley splittings in Si/SiGe quantum dots with a germanium spike in the silicon well. *Phys. Rev. B* **104**, 085406 (2021).
28. Paquelet Wuetz, B. et al. Atomic fluctuations lifting the energy degeneracy in Si/SiGe quantum dots. *Nat. Commun.* **13**, 7730 (2022).
29. Mi, X., Péterfalvi, C. G., Burkard, G. & Petta, J. R. High-resolution valley spectroscopy of Si quantum dots. *Phys. Rev. Lett.* **119**, 176803 (2017).
30. Borjans, F. et al. Probing the variation of the intervalley tunnel coupling in a silicon triple quantum dot. *PRX Quantum* **2**, 020309 (2021).
31. Seidler, I. et al. Conveyor-mode single-electron shuttling in Si/SiGe for a scalable quantum computing architecture. *NPJ Quantum Inf.* **8**, 100 (2022).
32. Burkard, G., Ladd, T. D., Pan, A., Nichol, J. M. & Petta, J. R. Semiconductor spin qubits. *Rev. Mod. Phys.* **95**, 025003 (2023).
33. Langrock, V. et al. Blueprint of a scalable spin qubit shuttle device for coherent mid-range qubit transfer in disordered Si/SiGe/SiO_2. *PRX Quantum* **4**, 020305 (2023).
34. Xue, R. et al. Si/SiGe QuBus for single electron information-processing devices with memory and micron-scale connectivity function. *Nat. Commun.* **15**, 2296 (2024).
35. Thorbeck, T. & Zimmerman, N. M. Formation of strain-induced quantum dots in gated semiconductor nanostructures. *AIP Adv*. **5**, 087107 (2015).
36. Corley-Wiciak, C. et al. Lattice deformation at submicron scale: X-ray nanobeam measurements of elastic strain in electron shuttling devices. *Phys. Rev. Appl.* **20**, 024056 (2023).
37. Zajac, D. M., Hazard, T. M., Mi, X., Wang, K. & Petta, J. R. A reconfigurable gate architecture for Si/SiGe quantum dots. *Appl. Phys. Lett.* **106**, 223507 (2015).
38. Scarlino, P. et al. Dressed photon-orbital states in a quantum dot: intervalley spin resonance. *Phys. Rev. B* **95**, 165429 (2017).
39. Mi, X. et al. A coherent spin-photon interface in silicon. *Nature* **555**, 599–603 (2018).
40. Borjans, F., Zajac, D., Hazard, T. & Petta, J. Single-spin relaxation in a synthetic spin-orbit field. *Phys. Rev. Appl.* **11**, 044063 (2019).
41. Hollmann, A. et al. Large, tunable valley splitting and single-spin relaxation mechanisms in a Si/Si_xGe_{1-x} quantum dot. *Phys. Rev. Appl.* **13**, 034068 (2020).
42. Chen, E. H. et al. Detuning axis pulsed spectroscopy of valley-orbital states in Si/Si-Ge quantum dots. *Phys. Rev. Appl.* **15**, 044033 (2021).
43. Bussmann, E. et al. Atomic-layer doping of SiGe heterostructures for atomic-precision donor devices. *Phys. Rev. Mater.* **2**, 066004 (2018).
44. Boykin, T. B. et al. Valley splitting in strained silicon quantum wells. *Appl. Phys. Lett.* **84**, 115–117 (2004).
45. Boykin, T. B. et al. Valley splitting in low-density quantum-confined heterostructures studied using tight-binding models. *Phys. Rev. B* **70**, 165325 (2004).
46. Kharche, N., Prada, M., Boykin, T. B. & Klimeck, G. Valley splitting in strained silicon quantum wells modeled with 2° miscuts, step disorder, and alloy disorder. *Appl. Phys. Lett.* **90**, 092109 (2007).
47. Friesen, M. & Coppersmith, S. N. Theory of valley-orbit coupling in a Si/SiGe quantum dot. *Phys. Rev. B* **81**, 115324 (2010).
48. Zhang, L., Luo, J.-W., Saraiva, A., Koiller, B. & Zunger, A. Genetic design of enhanced valley splitting towards a spin qubit in silicon. *Nat. Commun.* **4**, 2396 (2013).
49. Dyck, O. et al. Accurate quantification of Si/SiGe interface profiles via atom probe tomography. *Adv. Mater. Interfaces* **4**, 1700622 (2017).
50. Koelling, S., Stehouwer, L. E., Paquelet Wuetz, B., Scappucci, G. & Moutanabbir, O. Three-dimensional atomic-scale tomography of buried semiconductor heterointerfaces. *Adv. Mater. Interfaces* **10**, 2201189 (2023).
51. Losert, M. P. et al. Practical strategies for enhancing the valley splitting in Si/SiGe quantum wells. *Phys. Rev. B* **108**, 125405 (2023).
52. Evans, P. G. et al. Nanoscale distortions of Si quantum wells in Si/SiGe quantum-electronic heterostructures. *Adv. Mater.* **24**, 5217–5221 (2012).
53. Wang, G., Song, Z.-G., Luo, J.-W. & Li, S.-S. Origin of giant valley splitting in silicon quantum wells induced by superlattice barriers. *Phys. Rev. B* **105**, 165308 (2022).
54. Voigtländer, B. Fundamental processes in Si/Si and Ge/Si epitaxy studied by scanning tunneling microscopy during growth. *Surf. Sci. Rep.* **43**, 127–254 (2001).
55. Jernigan, G. G., Thompson, P. E. & Silvestre, C. L. Ge segregation during the initial stages of $Si_{1-x}Ge_x$ alloy growth. *Appl. Phys. Lett.* **69**, 1894–1896 (1996).
56. Uberuaga, B. P., Leskovar, M., Smith, A. P., Jónsson, H. & Olmstead, M. Diffusion of Ge below the Si(100) surface: theory and experiment. *Phys. Rev. Lett.* **84**, 2441–2444 (2000).
57. Qin, X. R., Swartzentruber, B. S. & Lagally, M. G. Scanning tunneling microscopy identification of atomic-scale intermixing on Si(100) at submonolayer Ge coverages. *Phys. Rev. Lett.* **84**, 4645–4648 (2000).
58. Bogusławski, P. & Bernholc, J. Surface segregation of Ge at SiGe(001) by concerted exchange pathways. *Phys. Rev. Lett.* **88**, 166101 (2002).
59. Lu, Z.-Y., Wang, C. & Ho, K. Mixed SiGe ad-dimer on Si(001): diffusion triggers intermixing. *Surf. Sci.* **506**, L282–L286 (2002).
60. Hannon, J. B., Copel, M., Stumpf, R., Reuter, M. C. & Tromp, R. M. Critical role of surface steps in the alloying of Ge on Si(001). *Phys. Rev. Lett.* **92**, 216104 (2004).
61. Akis, R. & Ferry, D. Kinetic lattice Monte Carlo simulations of germanium epitaxial growth on the silicon (100) surface incorporating Si-Ge exchange. *J. Vac. Sci. Technol. B* **23**, 1821–1825 (2005).
62. Zipoli, F. et al. First principles study of Ge/Si exchange mechanisms at the Si(001) surface. *Appl. Phys. Lett.* **92**, 191908 (2008).

63. Bussmann, E. & Swartzentruber, B. Ge diffusion at the Si(100) surface. *Phys. Rev. Lett.* **104**, 126101 (2010).
64. Hsu, J. W. P., Fitzgerald, E. A., Xie, Y. H., Silverman, P. J. & Cardillo, M. J. Surface morphology of relaxed Ge_xSi_{1-x} films. *Appl. Phys. Lett.* **61**, 1293–1295 (1992).
65. Jesson, D., Chen, K., Pennycook, S., Thundat, T. & Warmack, R. Mechanisms of strain induced roughening and dislocation multiplication in Si_xGe_{1-x} thin films. *J. Electron. Mater.* **26**, 1039–1047 (1997).
66. Fitzgerald, E. & Samavedam, S. Line, point and surface defect morphology of graded, relaxed GeSi alloys on Si substrates. *Thin Solid Films* **294**, 3–10 (1997).
67. Jernigan, G. G. & Thompson, P. E. Scanning tunneling microscopy of SiGe alloy surfaces grown on Si(100) by molecular beam epitaxy. *Surf. Sci.* **516**, 207–215 (2002).
68. Liu, Y. et al. Strain relaxation from annealing of SiGe heterostructures for qubits. *J. Appl. Phys*. **134**, 035302 (2023).
69. Jones, D., Pelz, J., Xie, Y., Silverman, P. & Gilmer, G. Enhanced step waviness on SiGe(001)-(2 × 1) surfaces under tensile strain. *Phys. Rev. Lett.* **75**, 1570 (1995).
70. Yitamben, E. et al. Heterogeneous nucleation of pits via step pinning during si (100) homoepitaxy. *N. J. Phys.* **19**, 113023 (2017).
71. Tersoff, J., Phang, Y. H., Zhang, Z. & Lagally, M. G. Step-bunching instability of vicinal surfaces under stress. *Phys. Rev. Lett.* **75**, 2730–2733 (1995).
72. Ebner, C., Jones, D. E. & Pelz, J. P. Equilibrium configuration of atomic steps on vicinal Si(001) surfaces with external biaxial strain. *Phys. Rev. B* **56**, 1581–1588 (1997).
73. Alerhand, O. L., Vanderbilt, D., Meade, R. D. & Joannopoulos, J. D. Spontaneous formation of stress domains on crystal surfaces. *Phys. Rev. Lett.* **61**, 1973–1976 (1988).
74. Tromp, R. M. & Reuter, M. C. Wavy steps on Si(001). *Phys. Rev. Lett.* **68**, 820–822 (1992).
75. Parsons, J., Parker, E. H., Leadley, D. R., Grasby, T. & Capewell, A. D. Misfit strain relaxation and dislocation formation in supercritical strained silicon on virtual substrates. *Appl. Phys. Lett*. **91**, 189902–189902-1 (2007).
76. Schelling, C., Springholz, G. & Schäffler, F. Kinetic vs. strain-induced growth instabilities on vicinal Si(001) substrates. *Thin Solid Films* **380**, 20–24 (2000).
77. Barlow, R. J. *In:* Statistics: a guide to the use of statistical methods in the physical sciences. Vol. 29 (John Wiley & Sons, 1993).
78. Gamble, J. K. et al. Multivalley effective mass theory simulation of donors in silicon. *Phys. Rev. B* **91**, 235318 (2015).
79. Van de Walle, C. G. & Martin, R. M. Theoretical calculations of heterojunction discontinuities in the Si/Ge system. *Phys. Rev. B* **34**, 5621–5634 (1986).
80. Hesthaven, J. S. & Warburton, T. *In:* Nodal discontinuous galerkin methods (Springer, 2008).

Acknowledgements

The authors thank R. Butera and C. Richardson of University of Maryland, C. Carter, Emeritus Professor U. of Connecticut, and T. Lu at Sandia National Laboratories for thought-provoking discussions. This work was performed at the Center for Integrated Nanotechnologies, an Office of Science User Facility operated for the U.S. Department of Energy (DOE) Office of Science. Research supported as part of μ-ATOMS, an Energy Frontier Research Center funded by the U.S. Department of Energy (DOE), Office of Science, Basic Energy Sciences (BES), under award DE-SC0023412 (data analysis and manuscript preparation). Sandia National Laboratories is a multi-mission laboratory managed and operated by National Technology and Engineering Solutions of Sandia, LLC, a wholly-owned subsidiary of Honeywell International, Inc., for the U.S. DOE's National Nuclear Security Administration under contract DE-NA-0003525. This paper describes objective technical results and analysis. Any subjective views or opinions that might be expressed in the paper do not necessarily represent the views of the U.S. Department of Energy or the United States Government.

Author contributions

L.F. Peña: investigation, formal analysis, writing—review and editing; J.C. Koepke: investigation, writing—review and editing; A Mounce: software; A.D. Baczewski: software, writing—review and editing; N.T. Jacobson: conceptualization, theoretical analysis, software, writing—original draft, funding acquisition, project administration; E. Bussmann: conceptualization, formal analysis, writing—original draft, funding acquisition, project administration.

Competing interests

The authors declare no competing interests.

Additional information

Supplementary information The online version contains supplementary material available at https://doi.org/10.1038/s41534-024-00827-8.

Correspondence and requests for materials should be addressed to N. Tobias Jacobson or Ezra Bussmann.

Reprints and permissions information is available at http://www.nature.com/reprints

Publisher's note Springer Nature remains neutral with regard to jurisdictional claims in published maps and institutional affiliations.

Open Access This article is licensed under a Creative Commons Attribution 4.0 International License, which permits use, sharing, adaptation, distribution and reproduction in any medium or format, as long as you give appropriate credit to the original author(s) and the source, provide a link to the Creative Commons licence, and indicate if changes were made. The images or other third party material in this article are included in the article's Creative Commons licence, unless indicated otherwise in a credit line to the material. If material is not included in the article's Creative Commons licence and your intended use is not permitted by statutory regulation or exceeds the permitted use, you will need to obtain permission directly from the copyright holder. To view a copy of this licence, visit http://creativecommons.org/licenses/by/4.0/.

© The Author(s) 2024